Unsteady 3D Post-Stall Aerodynamics Accounting for Effective Loss in Camber Due to Flow Separation

Aritras Roy, Rinku Mukherjee

Abstract—The current study couples a quasi-steady Vortex Lattice Method and a camber correcting technique, 'Decambering' for unsteady post-stall flow prediction. The wake is force-free and discrete such that the wake lattices move with the free-stream once shed from the wing. It is observed that the time-averaged unsteady coefficient of lift sees a relative drop at post-stall angles of attack in comparison to its steady counterpart for some angles of attack. Multiple solutions occur at post-stall and three different algorithms to choose solutions in these regimes show both unsteadiness and non-convergence of the iterations. The distribution of coefficient of lift on the wing span also shows sawtooth. Distribution of vorticity changes both along span and in the direction of the free-stream as the wake develops over time with distinct roll-up, which increases with time.

Keywords—Post-stall, unsteady, wing, aerodynamics.

I. INTRODUCTION

IT has been long established that panel methods, such as the Discrete vortex element method (DVEM) for simulating airfoils or the Vortex Lattice Method (VLM) for simulating wings, can predict aerodynamic coefficients quite reliably at pre-stall angles of attack. For post-stall angles of attack, methods that incorporate viscosity and predict flow separation, such as Reynolds Averaged Navier-Stokes (*RANS*) solver, Large Eddy simulation (*LES*) and Direct Numerical Simulation (*DNS*) take a large amount of time and computational resources. Even then, predictions from such methods at high angles of attack exhibit significant variations as has been discussed in [1]. Hence, several approaches utilising a strip theory approach along with panel methods have been tried to predict post-stall aerodynamic coefficients.

One of the approaches involves correction of the circulation strength, Γ of the bound vortex filament. Tani [2] was the first to try such a method. He implemented a LLT formulation with 2D non-linear lift curve slope data as input to account for stall. His method worked upto the max C_l but his method didn't work once a particular section attained stall. In other words, the method was unable to handle the negative slope in the C_l-α curve that is seen beyond the max C_l.

Schairer [3] developed a similar method, where he used a trial and error method to find solutions. He demonstrated the presence of multiple solutions at post-stall angles when

Aritras Roy is a PhD Scholar, Applied Mechanics, Indian Institute of Technology Madras, Chennai, India-600036 (e-mail: aritrasroy73@gmail.com).

Rinku Mukherjee is Assistant Professor, Applied Mechanics, Indian Institute of Technology Madras, Chennai, India-600036 (e-mail: rinku@iitm.ac.in).

the C_l-α curve has a negative slope. He also observed that over a narrow range of α, asymmetric solutions were possible and commented that this could be the reason for violent roll moments.

Pizkin and Lewinsky [4] used a vortex lattice method containing a single vortex ring at each section with an unsteady wake. Their results showed the existence of sawtooth in section C_l distributions along the span of the wing. Their results also exhibited hysteresis with increasing and decreasing α showing the dependency of the solution on starting conditions. The stall hysteresis was also linked with aspect ratio of the wing and the negative slope of the non-linear data. The authors reported the presence of asymmetric solutions as well as multiple solutions.

Anderson [5] developed a lifting line theory that accounted for non-linearity. The authors didn't find asymmetric solutions but found multiple solutions at post-stall. Post stall solutions upto 50° were calculated but the author cautions for the use of LLT for such high angles of attack. Mccormick [6] used a non-linear LLT and observed that no asymmetry existed. The authors studied the roll of the wing for cases close to stall.

The second approach utilized an alpha correction and was tried by Tseng and Lan [7]. The α at each section is changed depending on the difference between potential and viscous coefficients of lift ($\Delta C_l = (C_l)_{pot} - (C_l)_{visc}$). The authors used their methods to study fighter plane configurations. They found the point of separation from ΔC_l and then calculated the α correction using this point of separation information. Van Dam [8] implemented a similar methodology with a slight change in the approach by linking the ΔC_l directly to the α correction. The authors were concerned with developing a rapid predictive tool even at post-stall for conceptual and preliminary design stages. The authors were particularly interested in calculating the max C_L. Different airfoil data could be given as input for different sections of the wing.

In the 'decambering' approach developed by Mukherjee and Gopalarathnam [9], the effective loss in camber of the wing-section (local airfoil) due to flow separation at high angles of attack is accounted for using the residuals, i.e. ΔC_l and ΔC_m. This is the first instance, where C_m is also used. The change in camber is characterised by two linear functions. Based on the ΔC_l and ΔC_m the camber at each section is corrected. This results in a correction of both the Γ (and as a result the C_l and C_m) and α at each iteration, thereby establishing a direct relationship between the two.

Both Tseng and Lan [7] and Mukherjee and Gopalarathnam [9] implemented a physical change to

World Academy of Science, Engineering and Technology
International Journal of Aerospace and Mechanical Engineering
Vol:12, No:6, 2018

the section in which correction is being done, the former [7] in the form of a variation in the separation point and the latter [9] in the form of camber correction. The implication here is that a viscous correction of Γ or α has to follow or be followed by some physical change, as would happen in a real flow when Γ or α changes.

It is important to note here that a comprehensive understanding of strip theory stall predictions in an unsteady setting is not yet attained. The work reported in this paper lays the foundation tools for gaining further insights in this direction. The primary objective of this work is to extend the in-house Decambering methodology to model *unsteady* post-stall flow by coupling an Unsteady Vortex Lattice Method with the Decambering methodology.

II. NUMERICAL METHODOLOGY

The objective of this section is to couple the in-house decambering method, developed by Mukherjee et al. [9] to an Unsteady Vortex Lattice Method (UVLM). The decambering method ensures that aerodynamic coefficients predicted using the UVLM accounts for viscous effects in a way similar to aerodynamic coefficients predicted in a viscous domain. The decambering method requires an airfoil's 2D steady $C_l - \alpha$ and $C_m - \alpha$ as input. Thus utilizing 2D steady data, 3D unsteady data can be predicted.

1) Unsteady Vortex Lattice Method: The UVLM is used to predict transient aerodynamic coefficients $C_L(t)$ and $C_M(t)$. The wake behind the wing is force-free for an unsteady case. The evolution of the wake, as seen in Fig. 1, at each time step is calculated and the influence on the wing is studied.
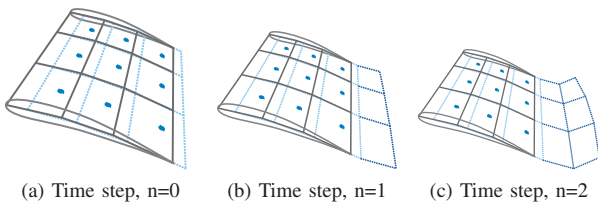
(a) Time step, n=0   (b) Time step, n=1   (c) Time step, n=2

Fig. 1 Wake evolution in the UVLM

2) Wake Vortex Filament with Finite Core: The velocity induced by the vortex filament, $\overrightarrow{v}_{ind}$, is inversely proportional to the distance between the filament and the point at which velocity is induced. When this distance becomes too small, numerical singularity arises. In order to avoid such singularity, a finite Rankine vortex-core is introduced around the wake vortex filament as seen in Fig. 2b and the corresponding induced velocities are calculated avoiding singulrities is given by (1). For a vortex filament of length r_0, a core of length $l_c = r_0 + r_c$ is used, r_c being the radius of the core.

$$\overrightarrow{v}_{ind} = \begin{cases} \frac{\Gamma}{4\pi} \frac{\overrightarrow{r_1} \times \overrightarrow{r_2}}{|\overrightarrow{r_1} \times \overrightarrow{r_2}|^2} \overrightarrow{r_0} \cdot \left(\frac{\overrightarrow{r_1}}{r_1} - \frac{\overrightarrow{r_2}}{r_2} \right), & r > r_c \\ \frac{\Gamma}{4\pi} \frac{\overrightarrow{r_1} \times \overrightarrow{r_2}}{|\overrightarrow{r_0}|^2 |\overrightarrow{r_c}|^2} \overrightarrow{r_0} \cdot \left(\frac{\overrightarrow{r_1}}{r_1} - \frac{\overrightarrow{r_2}}{r_2} \right), & 0 \leq r \leq r_c \end{cases} \quad (1)$$

(a) Velocity induced by   (b) Vortex core surrounding
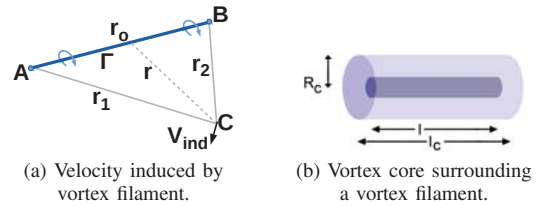vortex filament.   a vortex filament.

Fig. 2 Wake vortex filament

3) Wake Definition: The fixed horse shoe vortices in VLM are done away with and the wake is represented by freely evolving wake vortex rings. If the wing is assumed to start from rest, or if initially there is no fluid motion, then at the first time step there is no wake as shown in Fig. 1a. At each subsequent time-step the trailing edge bound vortex rings of the previous time-step are shed into the fluid stream as wake vortex rings as seen in Figs. 1b and 1c. The circulation of the recently shed wake vortex remains the same as that of the circulation of TE bound vortex rings from the previous time-steps. The distance travelled by the shed wake at each time-step is found by calculating the velocity induced on each of the 4 vertices, by the wings, wake and the free stream velocity and moving each vertex by a distance given by (2).

$$\overrightarrow{\Delta x} = \overrightarrow{V_v} \cdot \Delta t \quad (2)$$

Where,

$$\overrightarrow{V_v} = \overrightarrow{U_\infty} + \sum_{j=1}^{Npan} (\overrightarrow{v_{br}})_j + \sum_{k=1}^{NW_n} (\overrightarrow{v_{wr}})_k$$

n is the current time step index, with the first time step starting at n=0; NW_n=NY×n is the number of wake vortex rings at the particular time-step; v_{br} and v_{wr} are the velocity induced by a bound and wake vortex ring respectively; Npan is the total number of panels or bound vortex rings in the wing(s); U_∞ is the free stream velocity.

4) Circulation of Bound Vortex: The circulation of the wake and its position at any given time-step is known, which means the wake is no longer an unknown quantity and is calculated as shown in (3).

$$\sum_{j=1}^{Npan} (\overrightarrow{v_{br}} \cdot \hat{n}_i)_j + \sum_{k=1}^{NW_n} (\overrightarrow{v_{wr}} \cdot \hat{n}_i)_k + \overrightarrow{U_\infty} \cdot \hat{n}_i = 0 \quad (3)$$

The unknown quantity is the circulation of the bound vortex rings, Γ_{br}, which is given by (4) for the unsteady case.

$$[IC]_{(Npan \times Npan)} [\Gamma_{br}]_{(Npan \times 1)} = - \left[\left(\overrightarrow{U_\infty} + \overrightarrow{V_{wr}} \right) \cdot \hat{n} \right]_{(Npan \times 1)} \quad (4)$$

where,

$$\overrightarrow{V_{wr}} = \sum_{k=1}^{NW_n} (\overrightarrow{v_{wr}})_k$$

$\overrightarrow{V_{wr}}$ is the sum of velocity induced by all the wake vortex rings at a certain point.

World Academy of Science, Engineering and Technology
International Journal of Aerospace and Mechanical Engineering
Vol:12, No:6, 2018

5) Unsteady Aerodynamic Coefficients: The pressure difference across each panel, which has both steady and unsteady components is calculated using (5) followed by the force using (6). Finally, the transient coefficients of lift, $C_L(t)$ and pitching moment, $C_M(t)$ from the force.

$$\Delta p_{i,j} = \rho \left\{ \left(\overrightarrow{U_\infty} + \overrightarrow{V_{wr}} \right) \cdot (\overrightarrow{\tau_c})_{i,j} \, \frac{\delta}{\delta x} \Gamma_{br} \right\} +$$
$$\rho \left\{ \left(\overrightarrow{U_\infty} + \overrightarrow{V_{wr}} \right) \cdot (\overrightarrow{\tau_s})_{i,j} \, \frac{\delta}{\delta y} \Gamma_{br} + \frac{\delta}{\delta t} \Gamma_{br} \right\} \qquad (5)$$

where,

$$\frac{\delta}{\delta x} \Gamma_{br} = \frac{\Gamma_{i,j}^n - \Gamma_{i-1,j}^n}{\Delta c_{i,j}}; \qquad \frac{\delta}{\delta y} \Gamma_{br} = \frac{\Gamma_{i,j}^n - \Gamma_{i,j-1}^n}{\Delta b_{i,j}};$$
$$\frac{\delta}{\delta t} \Gamma_{br} = \frac{\Gamma_{i,j}^n - \Gamma_{i,j}^{n-1}}{\Delta t}$$

i, j being the panel indices, $\Delta c, \Delta b$ are the average length of the panel and τ_c, τ_s are the panel unit vectors in the direction of the panel chord and span respectively. Γ_{br} is the circulation of a bound vortex ring. $\Gamma_{i,j}^n$ represents the circulation of the bound vortex ring at panel i, j at time step n, the subscript 'br' has been omitted for brevity. Δt is the time increment between successive time-steps and ρ is the density of the fluid.

The force on each panel of area, $\Delta s = \Delta c \times \Delta b$, is given by (6).

$$\Delta \overrightarrow{F_{i,j}} = (\Delta p_{i,j} \Delta s_{i,j}) \, \hat{n}_{i,j} \qquad (6)$$

Let $\overrightarrow{p_{i,j}} = \overrightarrow{U_\infty} \times (\overrightarrow{\tau_c})_{i,j}$. Then the lift of the entire wing is given by (7) and C_L and C_M can be calculated from this.

$$\overrightarrow{L} = \sum_{i=1}^{NX} \sum_{j=1}^{NY} (\Delta L_{i,j}) = \sum_{i=1}^{NX} \sum_{j=1}^{NY} \left(\Delta \overrightarrow{F_{i,j}} \cdot \frac{\overrightarrow{p_{i,j}}}{|\overrightarrow{p_{i,j}}|} \right) \qquad (7)$$

A. Decambering

The decambering methodology developed by Mukherjee et al. [9] is similar in implementation to the Nascent Vortex method presented here. The decambering method tries to account for the discrepancy between the inviscid aerodynamic coefficients $(C_l)_{pot}$ and $(C_m)_{pot}$ and the viscous aerodynamic coefficients $(C_l)_{visc}$ and $(C_m)_{visc}$ after flow separation by modifying the effective camber of the lifting line.

1) 2D Methodology: The typical flow past an airfoil at low angles of attack consists of a thin attached boundary layer on the airfoil surface as seen in Fig. 3a. With increasing angles of attack, the boundary layer thickens on the upper surface and finally separates as shown in Fig. 3b. Now the flow no longer follows the camber of the airfoil, i.e. the effective camber that the airfoil enforces on the flow is different from the actual camber. If this change in effective camber can be quantified then the difference $\Delta C_l = (C_l)_{visc} - (C_l)_{pot}$ and $\Delta C_m = (C_m)_{visc} - (C_m)_{pot}$ can be evaluated. Conversely, if this difference is known then the effective camber can be calculated.

The change in effective camber is characterised by two linear functions, δ_1 and δ_2 placed on the camber of the airfoil at positions x_1 and x_2 respectively as shown in Fig. 4 and calculated using the residuals, ΔC_l & ΔC_m using (8).
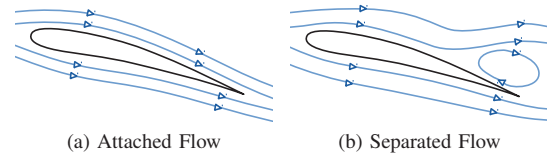

(a) Attached Flow   (b) Separated Flow

Fig. 3 Flow over an airfoil

$$\delta_1 = \frac{[\Delta C_l - 2(\pi - \theta_2) + 2sin\theta_2]\delta_2}{2\pi}$$
$$\delta_2 = \frac{\Delta C_m}{\frac{1}{4}sin2\theta_2 - \frac{1}{2}sin\theta_2} \qquad (8)$$

where,

$$\theta_2 = cos^{-1}\left(1 - \frac{2x_2}{c}\right); \qquad \frac{x_2}{c} = 0.8$$
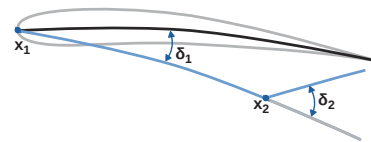

Fig. 4 Decambering Functions

2) 3D Methodology: A multi-dimensional Newton iteration is used for a 3D wing to find the section-wise decambering, δ_1 and δ_2 using which, the local target angle of attack, α_t at each section and the corresponding sectional target viscous aerodynamic coefficients, $(C_l)_t$ and $(C_m)_t$ obtained from the input airfoil data corresponding to α_t and the predicted coefficients $(C_l)_s$ and $(C_m)_s$ using the decambered wing from potential theory are calculated. The objective here is to predict the decambering correctly so that the residuals are minimized.

3) Finding Local and Target Angle of Attack: The local angle of attack at each section is found by using (9).

$$\alpha_{sec} = \frac{(C_l)_{sec}}{2\pi} - \delta_1 - \delta_2\left[1 - \frac{\theta_2}{\pi} + \frac{sin\theta_2}{\pi}\right] + \alpha_{0l} \qquad (9)$$

where, α_{0l} is the zero lift angle of attack of the airfoil used. To find the local α_{sec} the coefficient of lift $(C_l)_{sec}$ and the decambering characteristics δ_1 and δ_2 has to be known.

To find the target alpha at a particular section the sectional C_{ls} and α_s are found. Then the δ_1 is perturbed and new values of sectional C_{ln} and α_n are generated. The slope of the line joining α_s, C_{ls} and α_n, C_{ln} is now calculated. The point at which this line meets the input data's $C_l - \alpha$ curve is noted. This point provides the target angle of attack (α_t) and target coefficient of lift (C_{lt}) for the particular section.

4) Handling Multiple Solutions: One of the effects of finding targets this way is that multiple solutions are obtained at times depending on the slope of the line. Three instances of the line intersecting with the input aerodynamic data is shown in Fig. 5. Lines L1 and L3 has only one solution, while line L2 three solutions.

In order to aid this selection, a logical switch called *lpoststall* is used at each section, which is set to *TRUE* or

World Academy of Science, Engineering and Technology
International Journal of Aerospace and Mechanical Engineering
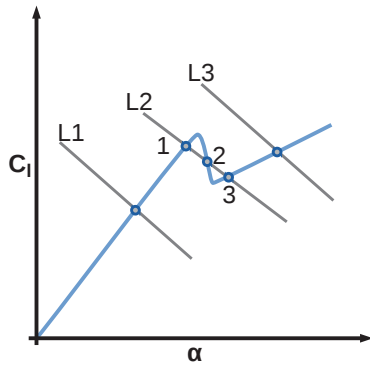Vol:12, No:6, 2018

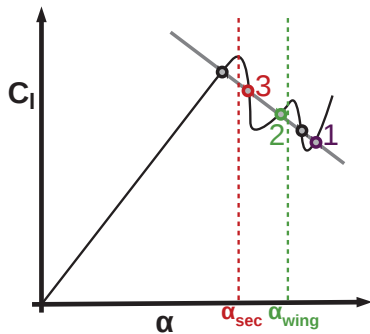Fig. 5 Inclined Trajectory Lines

Fig. 6 Multiple Solutions at post-stall angle of attack

FALSE if the section under consideration is stalled or unstalled. If there are multiple solutions at a particular section the status of this switch is checked. If it is *FALSE*, solution 1 is selected and if it is *TRUE*, solution 3 is selected as shown in Figs. 5 and 6.

Two other Multiple Solution Selection Methods (MSSM) have been proposed to circumvent this problem as listed below and as shown in Fig. 6.

MSSM 1: This method has been previously discussed as part of the decambering methodology. The solution is represented by the green point marked as "1".

MSSM 2: The intersection point whose α is closest to the wing α is chosen as the target, which is the green point marked as "2".

MSSM 3: The intersection point whose α is closest to the local α calculated from the previous iteration is chosen, which is the red point marked "3".

5) Iteration: The steps of the iteration to implement steady-state decambering method are listed here in brief.

1) Assume starting decambering, δ_1 & δ_2 values at all sections of the wing.
2) Compute aerodynamic coefficients of the decambered wing, $(C_l)_{inv}$ and $(C_m)_{inv}$ using Vortex Lattice Method.
3) Compute local effective AOA, α_{sec} of each decambered section.
4) Obtain target aerodynamic coefficients corresponding to α_{sec}, $(C_l)_{visc}$ and $(C_m)_{visc}$ from input airfoil data for each decambered section.
5) Calculate residuals $\Delta C_l = (C_l)_{visc} - (C_l)_{inv}$ & $\Delta C_m =$

$(C_m)_{visc} - (C_m)_{inv}$ using one of two schemes.
6) If the residuals are within tolerance, iteration has converged. The starting values of the decambering can be considered as the final values.
7) Else re-compute Jacobian. Solve $J.\delta x = -F$ to find δx. Update δ_1 & δ_2 and repeat from step 2.

B. Coupling Decambering and UVLM

Decambering is a steady method and as such utilizes steady 2D viscous aerodynamic coefficients as input to account for viscous effects. The circulation of the vortex rings, Γ_{br}, at each section is modified according to the input $(C_l)_{visc}$ and $(C_m)_{visc}$. In the UVLM the Γ_{br} at each time step is similarly modified. However while calculating the C_{ls} and C_{ms} from Γ_{br}, while iterating for a decambered solution, the unsteady part in (5) is ignored as we assume each section to be locally steady at that particular time-step. Once a converged solution is obtained the C_{ls} and C_{ms} at each section is recalculated, this time taking into account the unsteady part of (5). This way we obtain 3D unsteady data from 2D steady data.

III. Results

The unsteady C_L for a suddenly moving elliptic wing is compared with analytical results of Jones et al. [10] as seen in Fig. 7. A pretty close match is observed throughout except at $(U_\infty t)/c=0$. This is because the acceleration is infinite in the analytical model at $t = 0$. However, numerically only a finite acceleration can be applied.
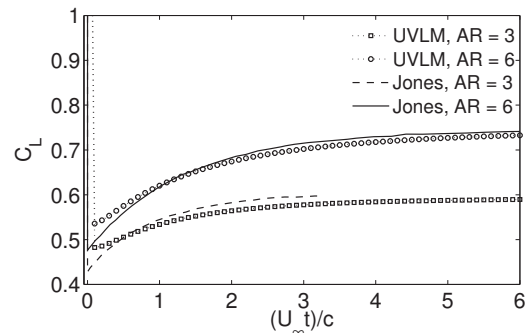

Fig. 7 Transient C_L of a suddenly moving elliptic wing

The unsteady C_L for a plunging wing at three different reduced frequencies, $k = 0.1, 0.3$ and 0.5 is compared with the results of Katz [11] as shown in Fig. 8.
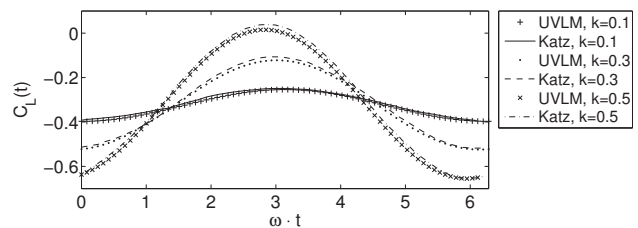

Fig. 8 Transient C_L of plunging wing

The computatinal expenditure of the code is evaluated by varying the three primary parameters, NX, NY and dt for

World Academy of Science, Engineering and Technology
International Journal of Aerospace and Mechanical Engineering
Vol:12, No:6, 2018

a wing that starts from rest and keeps moving at a constant velocity for 10 seconds. The time taken in seconds for each run is shown in Fig. 9. The simulations were run in a HP xw6600 workstation with 7.8 GB RAM and an Intel Xeon processor with 3.0 GHz processing speed containing 4 cores.
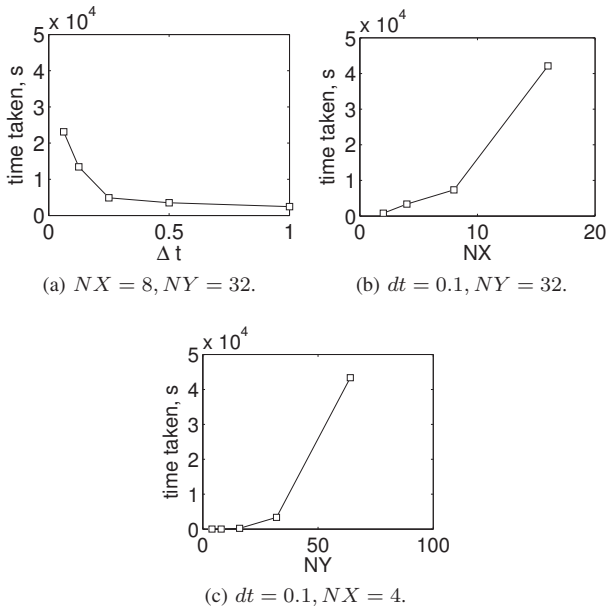

(a) $NX = 8, NY = 32$.

(b) $dt = 0.1, NY = 32$.

(c) $dt = 0.1, NX = 4$.

Fig. 9 Run time in seconds for varying parameter values

A suddenly moving wing of aspect ratio $AR = 9$ and $NACA4409$ section is studied for inviscid and decambered cases using UVLM developed for this purpose for $\Delta t = 0.1$. The $C_L - \alpha$ for such a case where the post-stall C_L values are calculated using the three different MSSMs is studied first for the steady case as shown in Fig. 10a.
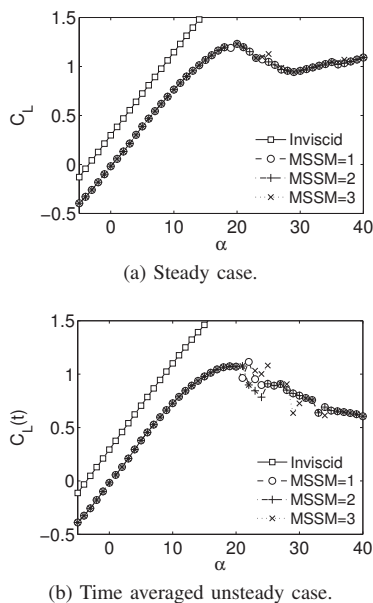

(a) Steady case.

(b) Time averaged unsteady case.

Fig. 10 C_l vs α for a rectangular NACA4409 wing. AR=9

For the unsteady case of the suddenly moving wing, the

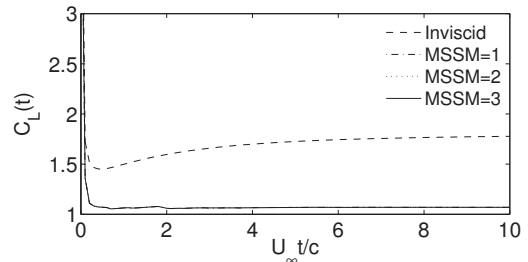Fig. 11 $C_L(t)$ of a suddenly moving NACA4409 wing, AR=9, $\alpha = 20°$.

angle of attack, α is varied from $-5°$ to $40°$ in steps of $1°$. The simulation at each angle of attack is run for 100 time-steps while the Δt is kept constant at 0.1. In order to compare unsteady case with that of the steady case, the $C_L(t)$ values at $(U_\infty t)/c > 7$ is averaged over time and the variation of these values over α and different MSSM is shown in Fig. 10b. The variation of the C_L with time is shown in Fig. 11, where the different MSSMs do not display any variations indicating there are no multiple solutions.

In Fig. 11 it is seen that the initial $C_L(t)$ value is quite high and then falls low before stabilising as time increases for the inviscid case. For the decambered case it seen that, the $C_L(t)$, falls below the inviscid $C_L(t)$ after the initial time step, however recovery of the $C_L(t)$ is minimal for the decambered case. It can be inferred that there are no multiple solutions as all three MSSM's select the same solution at all time steps. Similar plots for $\alpha = 30°$ and $40°$ can be seen in Fig. 12.
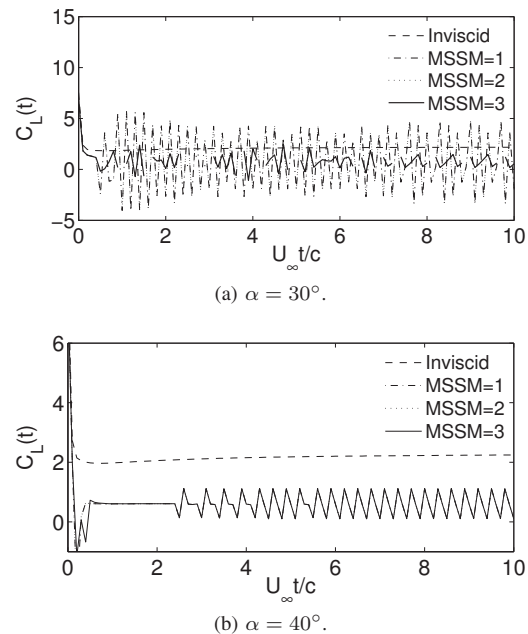

(a) $\alpha = 30°$.

(b) $\alpha = 40°$.

Fig. 12 $C_L(t)$ of a suddenly moving NACA4409 wing, AR=9

For $\alpha = 30°$ shown in Fig. 12a it can be seen that MSSM 1 and 2 have strong oscillations throughout. This is due to the unsteady part of the $C_L(t)$ kicking in when a particular section changes from one solution to the other there by causing a huge jump. It is seen that for MSSM=3 there are oscillations of a relatively smaller amplitude but it does not converge at

World Academy of Science, Engineering and Technology
International Journal of Aerospace and Mechanical Engineering
Vol:12, No:6, 2018

all time steps.

At $\alpha = 40°$ shown in Fig. 12b there are oscillations of a much smaller magnitude. The three MSSM keeping choosing the same solution suggesting that multiple solutions do not exist. It is interesting that at deep stall there are oscillations in $C_L(t)$ inspite of there being no multiple solutions.

The section C_l and effective α distribution along span of the suddenly moving wing for $\alpha = 30°$ and at time-step, t=10 is shown in Fig. 13. It is seen that the solution has sawtooth for both C_l and α for all three MSSM cases but MSSMs 1 and 2 select the same solution.
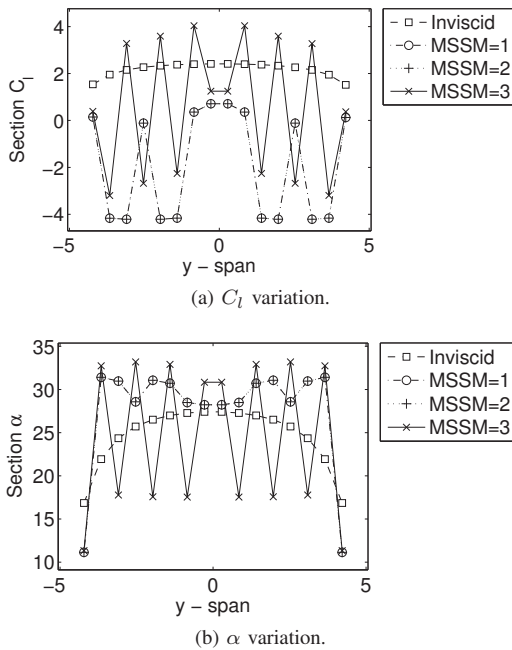

(a) C_l variation.

(b) α variation.

Fig. 13 Variation of different MSSMs, section: NACA4409, AR=9, $\alpha = 30°$, t=10

(a) C_l variation.

(b) Γ variation.

Fig. 14 Variation along span at different time-steps, section: NACA4409, AR = 9, $\alpha = 30°$

Fig. 15 Wake behind a 3D inviscid wing.

It should be noted the section α is pseudo-steady in nature as it does not have an unsteady component as the C_l has in (5). Thus, the section α can be directly related to the circulation of the blade at each time step but the unsteady component has to be taken into account in order to relate it to the section C_l.

The unsteady spanwise variation of section C_l and circulation, Γ, for 3 consecutive time-steps, t = 9.8, 9.9 and 10 is shown in Fig. 14 for $\alpha = 30°$ and using *MSSM* = 1. It is seen that at $t = 9.9$, both the section C_l and Γ peak but the root section sees minimum $C_l \approx 1$ and Γ suggesting that the root has stalled.

The wake that evolves behind a suddenly moving wing is shown in Fig. 15 for an inviscid wing at an $\alpha = 10°$. Wake roll-up can be be observed for $\frac{x}{c} \approx 6$ to 10, while the more recently shed vortex rings are found for $\frac{x}{c} \approx 0$ to 6. The circulation strength is highest for the vortex rings shed from the root for $\frac{x}{c} \geq 6$ while this is more uniformly distributed for $\frac{x}{c} \leq 6$.

The wake profile for a decambered wing for MSSM= 1 and $\alpha = 10°$ is shown in Fig. 16. It is seen that the circulation strength of the wake of the decambered wing is lower than that of the inviscid wing since decambering usually decreases the
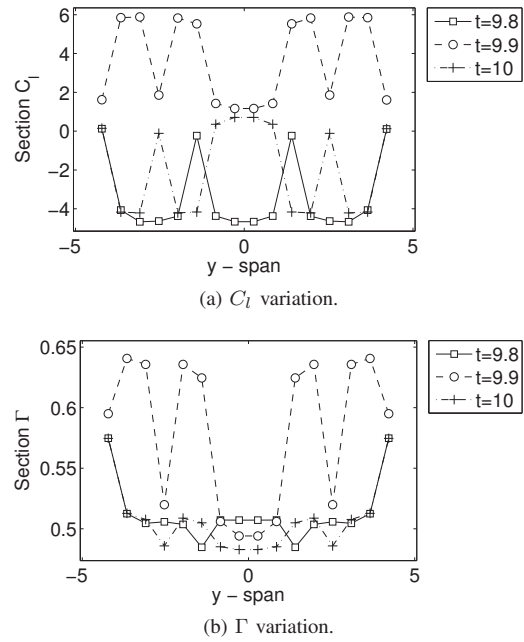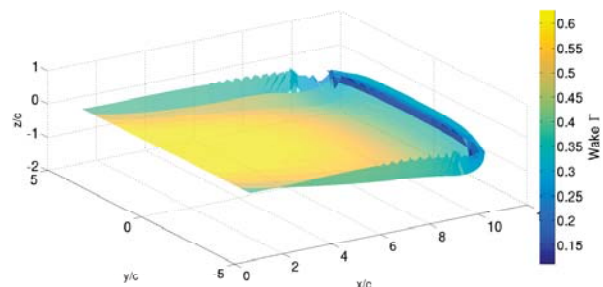
circulation strength of the bound vortex rings. The oscillations present in the wake vortices shed from the tips are suppressed for the decambered wing.

The 2D sections of the wakes, at $\alpha = 10°$ and MSSM= 1, are plotted to obtain a better idea of wake evolution. Longitudinal sections of the wake shed at the root, shown by the line I-I in Fig. 16, and the tip, represented by the line J-J in Fig. 16, are studied at $t = 10$ as shown in Fig. 17. The wake roll-up is more prominent in the root section. It is also seen
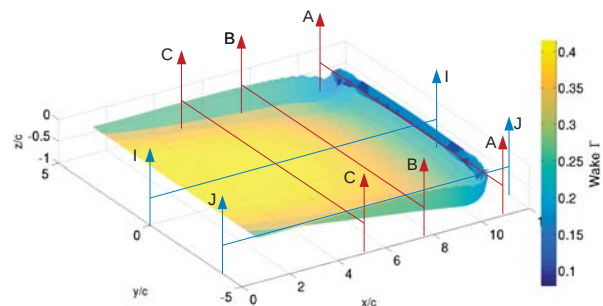

Fig. 16 Wake behind a 3D decambered wing

World Academy of Science, Engineering and Technology
International Journal of Aerospace and Mechanical Engineering
Vol:12, No:6, 2018

that the wake shed at the root moves downwards to a greater extent indicating that the lift is higher at the root section. The roll up of the wake from the decambered wing is lower when compared to the inviscid wing.
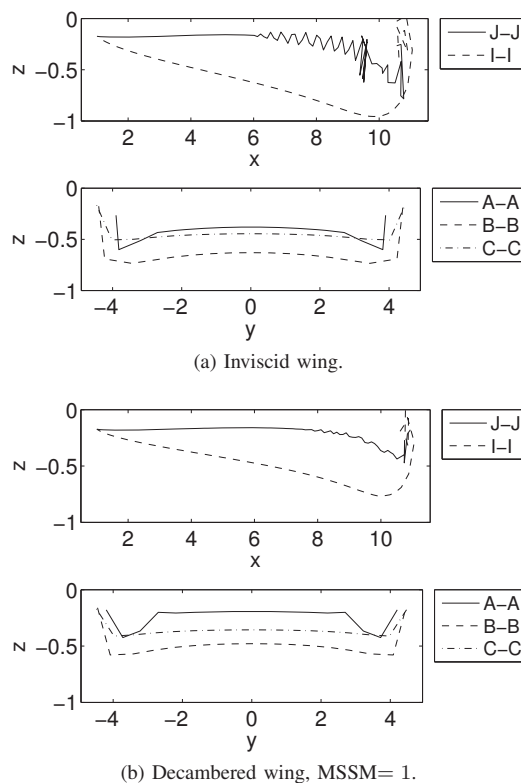

(a) Inviscid wing.

(b) Decambered wing, MSSM= 1.

Fig. 17 Cross section of wake at $t = 10$

Wake portions lateral to the wing and shed at $t = 0.1, 5$ and 7.5, denoted by lines A-A, B-B and C-C in Fig. 16, are allowed to evolve and their positions at $t = 10$ is studied in order to understand the evolution of the wake. The wake shed at $t = 0.1$, represented by A-A in Fig. 17, is the starting vortex, and almost has the highest circulation among the vortex filaments. It is seen that there is a dip in the filament as we move from the root sections towards the tip. This is due to the proximity to the tip vortex filaments. The starting vortex is the primary reason for the wake roll-up.

The wake shed at $t = 5$ and $t = 7.5$ is represented by B-B and C-C in Fig. 17. It is observed that B-B that was shed at an earlier time step has evolved more and has moved in the negative z-direction when compared to C-C. It is observed that there is a movement in the negative z-direction here too as we move from the root sections to the tip. Close to the tip the vortex filament moves up. The dip is primarily attributed to the tip vortex effect. Comparing Figs. 17a and 17b we can see that the tip vortex effect of the decambered wing is much lower than that of the inviscid wing. Overall decambering seems to give rise to a weaker wake.

IV. CONCLUSION

A novel nascent vortex method is developed, which accounts for viscous effects in an inviscid regime. Nascent Vortex (NV) methodology in tandem with basic Discrete vortex element method (DVEM) and Vortex lattice method (VLM) is used to predict the aerodynamic coefficients and separated flow characteristics of airfoils and wings, while using 2D aerodynamic coefficients as input. The addition of the nascent vortices enables the deviation of the aerodynamic coefficients from their original inviscid values.

A steady-state decambering methodology originally developed by Mukherjee et al. [9] is extended into the unsteady regime with specific interest in the unsteady post-stall regime. The unsteady vortex lattice method (UVLM) is implemented and decambering is coupled with it. Decambering had the capability of choosing a solution from multiple solutions arising at post-stall using a selection algorithm. Two new algorithms have been proposed and the variations in the final solution due to this change has been noted.

The UVLM captures the wake roll-up of the starting vortex and the tip vortices for both the inviscid and decambered cases. The decambered wing's wake has vortices of weaker circulation-strength when compared to the wake vortices from the inviscid wing.

REFERENCES

[1] C. L. Rumsey, J. P. Slotnick, M. Long, R. A. Stuever, and T.R. Wayman. Summary of the first aiaa cfd high-lift prediction workshop. *Journal of Aircraft*, 48(6):2068–2079, 2011.

[2] I Tani. A simple method of calculating the induced velocity of a monoplane wing. *Aero. Res. Inst., Tokyo Imperial Univ.*, 9(3), 1934.

[3] R. S. Schairer. Unsymmetrical lift distributions on a stalled monoplane wing. Master's thesis, California Institute of Technology, 1939.

[4] Stanley T. Piszkin and E. S. Levinsky. Nonlinear lifting line theory for predicting stalling instabilities on wings of moderate aspect ratio. Technical report, DTIC Document, 1976.

[5] John D. Anderson and Stephen Corda. Numerical lifting line theory applied to drooped leading-edge wings below and above stall. *Journal of Aircraft*, 17(12):898–904, 1980.

[6] Barnes W McCormick. An iterative non-linear lifting line model for wings with unsymmetrical stall. Technical report, SAE Technical Paper, 1989.

[7] Jing-Biau Tseng and C. Edward Lan. Calculation of aerodynamic characteristics of airplane configurations at high angles of attack. Technical Report NASA-CR-4182, Kansas Univ. Center for Research, Inc.; Flight Research Lab., 1988.

[8] C. P. Van Dam, J. C. Vander Kam, and J. K. Paris. Design-oriented high-lift methodology for general aviation and civil transport aircraft. *Journal of aircraft*, 38(6):1076–1084, 2001.

[9] Rinku Mukherjee and Ashok Gopalarathnam. Poststall prediction of multiple-lifting-surface configurations using a decambering approach. *Journal of Aircraft*, 43(3):660–668, 2006.

[10] Robert T. Jones. The unsteady lift of a wing of finite aspect ratio. Technical Report NACA-TN-682, National Advisory Committee for Aeronautics., 1940.

[11] J. Katz and A. Plotkin. *Low-Speed Aerodynamics*. Cambridge Aerospace Series. Cambridge University Press, 2001.

Aritras Roy <u>Academics</u>:
   BTech, Mechanical Engineering, Bengal Institute of Engineering and Technology, Kolkata, India, 2015
   ME, Power Engineering, Jadavpur University, India, 2017
   PhD Scholar, Applied Mechanics, Indian Institute of Technology Madras, Chennai, India 2017-present

Rinku Mukherjee <u>Academics</u>:
   BE, Civil Engg., Jadavpur University, India, 1998
   MS, Ocean Engg. and Naval Architecture, Indian Institute of Technology Kharagpur, India, 2001
   PhD, Aerospace Engg., North Carolina State University, USA, 2004
   Work Experience:
   Industry(1.5 years): MVSystems Inc., CO, USA
   Academia(10+ years): Faculty, Indian Institute of Technology Madras